Coastal Engineering 151 (2019) 1–9

Contents lists available at ScienceDirect

Coastal Engineering

journal homepage: www.elsevier.com/locate/coastaleng

High-resolution wave climate hindcast around Japan and its spectral representation

Tomoya Shimura*, Nobuhito Mori

Disaster Prevention Research Institute, Kyoto University, Kyoto, Japan

ARTICLE INFO

Keywords:
JRA-55
Long term wave hindcast
Ocean surface wave
Wave climate
Wave spectra

ABSTRACT

A 34-year high-resolution ocean surface wave climate hindcast around Japan is presented, and the wave climate around Japan is examined from a spectral point of view. The spectral wave model is forced by the sea surface wind data obtained from the JRA-55 atmospheric reanalysis. The wave climate hindcast is validated by comparing it with buoy observations around Japan. The correlation coefficient of the significant wave height is 0.9. The correlation coefficient of the mean wave period is 0.8 for the Japan Sea and Pacific side of eastern Japan and 0.7–0.8 for the Pacific side of western Japan. The wave climate is represented by temporal-mean two-dimensional wave spectra. The characteristics of the spectral wave climate are investigated by classifying them into three types. Distinctive characteristics of the mean wave spectra along the Japan Sea are narrower band widths for both the period and direction. The mean wave spectra along the Pacific side of eastern Japan are characterized by swells with a spectral peak propagating from the northeast. The distinctive spectral features corresponding to the Pacific side of western Japan are bi-modal peaks with long-period components typically generated by typhoons. The variability in the monthly mean wave spectra is examined using an empirical orthogonal function (EOF) analysis. In the winter, it is found that the wave height variability (EOF 1st mode) is related to wave direction variability (EOF 2nd mode) at locations 1000 km apart via the sea level pressure variance over the North Pacific. In the summer, the EOF 1st mode corresponding to the Pacific side locations is dominated by the variability in typhoon-generated swells. The spectral wave climate representation provides new insight into the wave climate around Japan with clear relationships between the atmospheric conditions, the wave height, direction, and period.

1. Introduction

It is becoming increasingly important to understand Earth's climate because of the potential impact of ongoing climate change on our society. The nature of the ocean surface wave climate has broad implications for coastal society because large populations live near the coastline; therefore an understanding of wave climate is important. Atmospheric reanalysis data is one of main tools available for investigating the climate of previous decades. In addition, a wave climate hindcast based on atmospheric reanalysis is useful for wave climate studies (e.g., Semedo et al., 2011; Shimura et al., 2013; Stopa et al., 2013) and is applicable to a wide range of coastal engineering projects. Beach morphology is strongly and globally affected by the wave climate in addition to sea level rise at historical climate (Barnard et al., 2015). Long-term wave climate hindcasts can be used for estimating beach morphology changes (Yates et al., 2013; Elshinnawy et al., 2017; Gainza et al., 2018). In addition, long-term wave climate hindcasts have been used to estimate ocean wave contributions to the long-term extreme global sea-level rise along coastlines (Melet et al., 2018), wave power resources (e.g., van Nieuwkoop et al., 2013; Morim et al., 2016), and coastal structure design (e.g., Gouldby et al., 2014). Therefore, reliable wave climate hindcasts based on atmospheric reanalysis are in great demand. The purposes of this study are to present a new wave climate hindcast around Japan and examine the wave climate characteristics based on this hindcast.

An example of a “global” long-term wave climate hindcast that has been used in a variety of fields is the ERA-Interim reanalysis (Dee et al., 2011) developed by the European Center for Medium Weather Forecast. Recently, several researchers (Chawla et al., 2013; Rascle and Ardhuin, 2013; Durrant et al., 2014; Perez et al., 2017) have conducted global wave climate hindcasts using the spectral wave model WAVEWATCH III (Tolman, 2014), forced by the CFSR atmospheric reanalysis (Saha et al., 2010) developed by the United States National Centers for Environmental Prediction. Mori et al. (2017) produced a global wave climate

* Corresponding author.
E-mail address: shimura.tomoya.2v@kyoto-u.ac.jp (T. Shimura).

https://doi.org/10.1016/j.coastaleng.2019.04.013
Received 28 September 2018; Received in revised form 25 January 2019; Accepted 22 April 2019
Available online 05 May 2019

hindcast data using the JRA-55 atmospheric reanalysis developed by the Japan Meteorological Agency (Kobayashi et al., 2015) and showed the accuracy and usefulness of these data. In general, recent global wave climate hindcasts have used a spatial resolution of approximately 0.5°, which is rather coarse for coastal applications. Therefore, the wave climate hindcasts along specific coastlines nested in the global domain are calculated using a higher spatial resolution than the one used to calculate the global wave climate hindcasts, i.e., approximately 4 arcmin (Chawla et al., 2013; Durrant et al., 2014; Perez et al., 2017). This study presents a higher resolution wave climate hindcast along the Japanese coast, which can be added to the global data-set of Mori et al. (2017). We evaluate the accuracy of the hindcast by comparison with buoy observations.

The wave climate is often described using bulk wave parameters, such as the significant wave height (H_s), mean wave period (T_{m01}), and mean wave direction (D_m) (e.g., Young et al., 2011; Shimura et al., 2013; Stopa et al., 2013; Hemer et al., 2013; Mentaschi et al., 2017). The wave climate can be more effectively studied using wave spectra because wave spectra contain more detailed information than bulk characteristic wave parameters do. Several authors have studied spectral wave climate representations. For example, Buckley (1988) calculated the long-term average of one-dimensional (frequency) wave spectra (climatic wave spectra) based on buoy observations taken around the United States and divided wave climates into steep and long states. Bromirski et al. (2005) investigated the wave energy variability along the United States west coast by separating the wave energy into short, intermediate, and long-period components based on the one-dimensional wave spectra obtained from buoy observations. The spectral wave climate has also been examined by several sea states using a clustering analysis of wave spectra (Boukhanovsky et al., 2007; Hamilton, 2010; Lucas et al., 2011). Innocentini et al. (2014); Portilla-Yandún et al. (2015) used the wave spectral partitioning method to detect a wave system from wave hindcast data and showed the climatic characteristics of representative wave systems. Portilla-Yandún et al. (2016); Portilla-Yandún (2018) showed the usefulness of wave spectral climate representations for relating the wave climate to climate circulation patterns and detecting wave generating sources. In this study, we examine the spectral wave climate characteristics using the long-term average of two-dimensional (frequency-direction) wave spectra. We focus on the spectral shape of the total wave energy during the target timeframe and not on each wave system (Portilla-Yandún et al., 2015). The variability in the spectral wave climate is estimated by applying empirical orthogonal function (EOF) analysis (Von Storch and Zwiers, 2002) to the monthly average of the two-dimensional wave spectra. Although the amount of data in the wave spectra is approximately 1 000 times larger than that contained in the bulk parameters, depending of the directional and frequency resolutions, data spanning several decades is worth saving and analyzing.

There have been only a limited number of studies of the long-term wave climate around the Japanese coast. The trend of the long-term wave climate around Japan has been estimated through observations (Sasaki, 2012), and a hindcast (Hatada and Yamaguchi, 2002). Shimura et al. (2016) found that the winter wave climate variability around Japan is closely associated with large-scale atmospheric patterns. There has been no study of the spectral wave climate around Japan, although Nagai (1997) investigated the observed wave spectral climate at two locations. This study investigates in detail the characteristics of the wave climate around Japan using a wave spectral climate representation obtained from a high-resolution wave climate hindcast.

2. Methodology

2.1. Wave climate hindcast

The wave climate hindcast is conducted using the spectral wave model WAVEWATCH III version 4.18 (Tolman, 2014). WAVEWATCH III is forced with six-hourly surface wind data and the monthly sea ice fields by JRA-55 atmospheric reanalysis data (Kobayashi et al., 2015). The experimental period is 34 years (1979–2012). The spatial resolution of JRA-55 is approximately 60 km. The monthly sea ice fraction data is linearly interpolated to daily data to obtain the WAVEWATCH III forcing data. The directional resolution is 10°, and the frequency space is 0.035–0.5 Hz, which is logarithmically discretized into 29 increments. The source terms from Ardhuin et al. (2010) (denoted as ST4 in WAVEWATCH III) are used as the input and dissipation terms. The global wave climate hindcast produced using the JRA-55 wind by Mori et al. (2017) did not store the spectral data for the boundary conditions of the nesting process. Thus, a new regional high resolution wave climate hindcast is conducted. With the exception of the spatial resolution, the global and regional configurations for WAVEWATCH III are identical. Therefore, the regional wave climate hindcast is considered to be a subset of the global one. The three domains are determined using a nesting process for the North Pacific domain (spatial resolution: 30 min/0.5°), western North Pacific domain (10 min/0.167°), and Japanese coastal domain (4 min/0.067°) (Fig. 1). The latitudes of the first (the North Pacific) domain range from 25°S-65°N, and the longitudes range from 110°E − 90°W. The latitudes of the second (the western North Pacific) domain range from 20°N-50°N, and the longitudes range from 117°E − 150°E; the boundary of the southeastern part of the domain is oblique to the longitude line. The boundary of the finest domain around Japan is approximately 100 km from the Japanese coast (see, Fig. 1). The bulk parameter outputs are available every hour. The spectral data are also available every hour at sites chosen based on observation data availability (see, section 2.2).

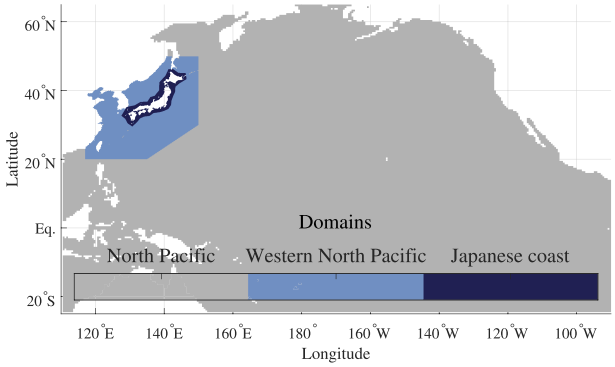

Fig. 1. The three computational domains.

Three regions, whose climate characteristics are chosen to represent the major wave climates, are frequently discussed in this paper. The three regions are: the Japan Sea side of Japan, Pacific side of eastern Japan, and Pacific side of western Japan. These three are hereafter denoted as the JS, PE, and PW regions, respectively. The winter months are December, January, and February (DJF), and the summer months are July, August, and September (JAS).

2.2. Validation of wave hindcast

To estimate the accuracy of the wave climate hindcast, a comparison with data obtained from buoy observations around Japan is pursued. We obtain long-term buoy observation data from the Nationwide Ocean Wave Information Network For Ports And Harbours (NOWPHAS; http://www.mlit.go.jp/kowan/nowphas/index_eng.html (Last access is November 2018)). A total of 43 locations within the finest domain whose depths are deeper than 30 m are selected for the comparison mainly focusing on deep water. The observations began in 1970, depending on the location. If there is a obvious data gap between before and after data missing period based on a visual inspection, data with shorter period is eliminated, although this elimination hardly impacts the results. The parameters chosen for the comparison are the

significant wave height (H_s) and mean wave period (T_{m01}). T_{m01} is denoted T_m for simplicity. Observed spectral data at a limited number of locations (five locations) and during a limited period (2001–2007 or 2002–2007) are available and used as a complement. The wave period parameter available from NOWPHAS is the significant wave period (T_s; the mean period of the highest one-third of the waves, Holthuijsen (2010)). The T_m values from the NOWPHAS observations are derived using the following equation: $T_m = 0.0083T_s^2 + 0.68T_s + 1.08$. The relationship between T_s and T_m is derived via an analysis of the spectral data of observation.

2.3. Analysis of spectral wave climate

The spectral wave climate is represented by temporal-mean two-dimensional (direction-frequency) wave spectra. The temporal-mean two-dimensional wave spectra ($\overline{F(\theta,f)}$) are defined as follows:

$$\overline{F(\theta,f)} = 1/n \sum_{t=1}^{n} F(\theta,f) \tag{1}$$

where θ is the direction, f is the frequency, and n is the number of time steps. Using $\overline{F(\theta,f)}$, the temporal-mean significant wave height ($\overline{H_s^{sp}}$) is defined as follows:

$$\overline{H_s^{sp}} = 4\sqrt{\iint \overline{F(\theta,f)}\, d\theta df} = \sqrt{\overline{H_s^2}} = \sqrt{\overline{H_s}^2 + \sigma_{H_s}^2} \tag{2}$$

where $\overline{H_s^{sp}}$ equals to the root mean square of H_s and $\sigma_{H_s}^2$ is the variance of H_s. Analogously with $\overline{H_s^{sp}}$, the temporal-mean mean period ($\overline{T_m^{sp}}$) and mean direction ($\overline{D_m^{sp}}$) are defined as follows:

$$\overline{T_m^{sp}} = \left(\frac{\iint f\bar{F} d\theta df}{\iint \bar{F} d\theta df} \right)^{-1} = \left(\frac{\overline{H_s^2 f_m}}{\overline{H_s^2}} \right)^{-1} \tag{3}$$

$$\overline{D_m^{sp}} = \tan^{-1}\left(\frac{\iint \sin\theta \bar{F} d\theta df}{\iint \cos\theta \bar{F} d\theta df} \right) = \tan^{-1}\left(\frac{\overline{H_s^2 \sin D_m}}{\overline{H_s^2 \cos D_m}} \right) \tag{4}$$

where $f_m = 1/T_m$. $\overline{T_m^{sp}}$ and $\overline{D_m^{sp}}$ are equal to the mean values weighted by the squared H_s. Gainza et al. (2018) indicated that weighted mean wave parameters are more effective for an equilibrium beach planform than ordinary (not weighted) temporal-mean wave parameters. This can be because weighted mean wave parameters better represent mean wave states. $\overline{F(\theta,f)}$ -based mean wave parameters, which are equal to weighted mean wave parameters (as shown by equations (2)–(4)), correspond to the total wave energy in the target timeframe; $\overline{H_s^{sp}}$ can be converted to the total wave energy in the target timeframe ($\iint \sum F d\theta df$), but $\overline{H_s}$ is just a statistical value. The relationship among $\overline{H_s}$, $\overline{T_m}$, and $\overline{D_m}$ is not clear because averaging procedures for those variables are conducted independently. On the other hand, $\overline{H_s^{sp}}$, $\overline{T_m^{sp}}$, and $\overline{D_m^{sp}}$ have a clear relationship via $\bar{F}$ as described by equations (2)–(4). We consider $\overline{H_s^{sp}}$, $\overline{T_m^{sp}}$, and $\overline{D_m^{sp}}$ to be more appropriate for representing the wave climate (mean wave state) than ordinary mean statistics.

The differences between the $\overline{F(\theta,f)}$ -based temporal-mean and the ordinary temporal-mean are described below. Fig. 2 shows the values of $\overline{H_s^{sp}}$, $\overline{H_s}$, $\overline{T_m^{sp}}$, and $\overline{T_m}$ over a period of 34 years for the second computational (the western North Pacific) domain. $\overline{H_s^{sp}}$ is always larger than $\overline{H_s}$ as shown by equation (2). The differences (Fig. 2(b) (d)) are not spatially uniform and are larger where the variance of H_s is relatively larger compared with the ordinary mean. Fig. 2 shows the annual mean, and if the seasonal mean is examined, it can be seen that the spatial pattern changes because the inter-annual variance is more important than the seasonal variation (cycle). For example, the inter-annual tropical cyclone (TC) variance is large and leads to large differences in the TC passing zone during the summer.

The monthly variability in the spectral wave climate is obtained using empirical orthogonal function (EOF) analysis (Von Storch and Zwiers, 2002), which is also known as the principal component analysis. EOF analysis is widely used in climate science studies to derive the dominant patterns of variability in temporal-spatial space. In this study, dominant patterns of wave climate variability in temporal-wave spectral space are derived using EOF analysis. EOF analysis is applied to the root monthly mean wave spectra. The "root" monthly mean value is used in order to increase the applicability of EOF analysis because the EOF analysis assumes normal distribution and "root" monthly mean value is closer to normal distribution than monthly mean value. The procedure of EOF analysis is described simply as follows. The 34-year mean of each calendar month is subtracted from each monthly value for normalization; for example, 34-year mean during January is subtracted from each monthly value of January. Root monthly mean wave spectra is represented by $m \times n$ matrix ($\mathbf{F}$), where m is the number of wave components (the number of frequencies × the number of directions), and n is the number of months. The co-variance matrix ($\mathbf{V}$) is calculated by $\mathbf{V} = \mathbf{F}\mathbf{F}^{\mathrm{T}}/n$. The eigen value equation for $\mathbf{V}$ can be expressed as $\mathbf{V}\mathbf{z}_i = \lambda_i \mathbf{z}_i$ with the ith largest eigenvalue λ_i and the associated ith eigenvector $\mathbf{z}_i$. $\sqrt{\lambda_i}\mathbf{z}_i$ is denoted as the spectral pattern of ith EOF (unit is m/(s · rad) which is same as root monthly mean wave spectra). The spectral patterns of lower order (1st, 2nd, …) EOF represent dominant patterns of variability in the spectral wave climate. The time coefficient of ith EOF at a given month (t) is calculated by $eof_i(t) = \mathbf{F}(t)^{\mathrm{T}}\mathbf{z}_i/\sqrt{\lambda_i}$, where $\mathbf{F}(t)$ is $m \times 1$ vector of root monthly mean wave spectra at a given month. The eof_i is non-dimensional value. The mean and standard deviation of eof_i are 0 and 1, respectively. Larger value of eof_i indicates the spectral pattern at a month can be explained by that of ith EOF by a larger degree.

The relationship between the EOF of the wave spectra and the large-scale atmospheric conditions is analyzed using regression analysis. The monthly averaged mean sea level pressure (SLP) and wind vector are used to determine the atmospheric conditions. The monthly averaged value of SLP, u-component, or v-component wind at a month t ($y(t)$) is represented by $eof_i(t)$ using linear regression equation as follows:

$$\hat{y}(t) = a_1 eof_i(t) + a_0 \tag{5}$$

where $\hat{y}(t)$ is the estimated $y(t)$, and a_1 and a_0 are the regression coefficients determined using the least squares method. The spatial distribution of slope (a_1) is denoted as a regression map. The $eof_i(t)$ is non-dimensional value as describe above and thus a_1 has dimention same as SLP (hPa) or wind (m/s).

3. Results and discussion

3.1. Comparison with buoy observations

A comparison of the H_s values calculated from the hindcast and NOWPHAS buoy observational data is shown below. Fig. 3(a) and (b) show the correlation coefficient and root mean square error (RMSE) of the two-hourly H_s values between the hindcast and NOWPHAS, respectively. Fig. 3 also shows the $\overline{H_s^{sp}}$ values drawn in grayscale. The correlation coefficients are approximately 0.9 for nearly all of the locations; thus the accuracy is high. Some locations inside the steeply curved bay show smaller correlation coefficients of 0.5–0.7. This indicates that the wind and waves at such complex topographical locations cannot be resolved well by JRA-55 reanalysis or the current study's wave model. The RMSE values are less than 0.5 m at nearly all of the locations. The biases are −0.39 to 0.15 m (not shown in the figure). The results for the three representative locations in the JS, PW, and PE regions (Wajima, Hososima, and Kuji), which correspond to Nos. 21, 14, and 2 in Fig. 7 and Table 1, respectively, are shown in detail (Fig. 4). The correlation coefficients are 0.94, 0.90, and 0.89 for Wajima, Hososima, and Kuji, respectively. The biases are −0.14, −0.02, and −0.01 m, and the RMSE values are 0.36, 0.30, and 0.30 m, respectively. The percentile values (10, 50, 90, 99, and 99.99 percentiles), which have been treated as wave climate indicators in previous studies, are also plotted in Fig. 4 and show good agreement between the smaller and larger waves.

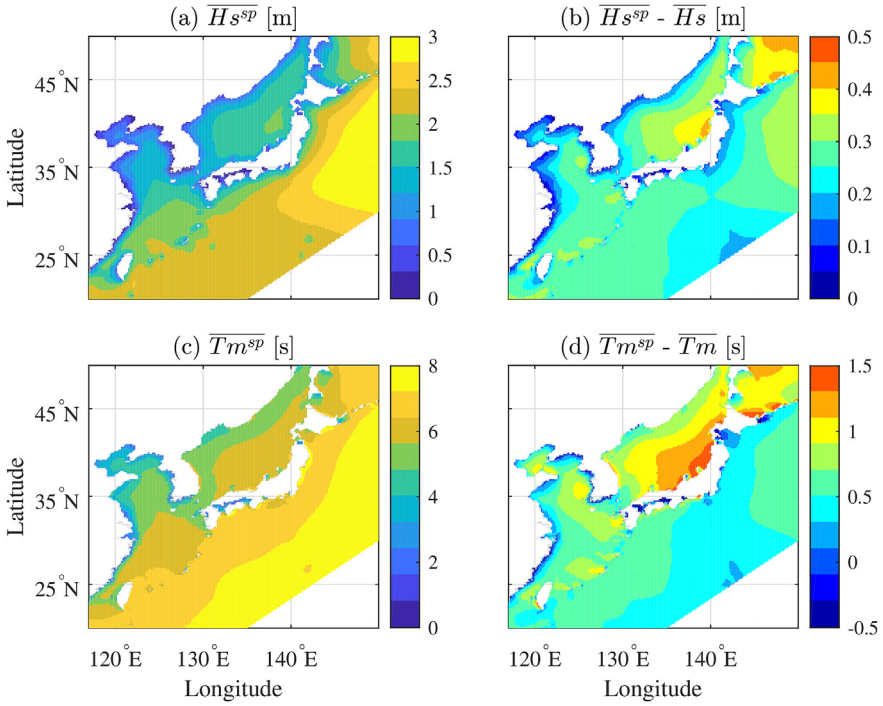

Fig. 2. Differences between $\overline{F(\theta,f)}$ -based temporal-mean and ordinary temporal-mean values over a period of 34 years. (a) $\overline{H_s^{sp}}$, (b) $\overline{H_s^{sp}}$ - $\overline{H_s}$, (c) $\overline{T_m^{sp}}$, and (d) $\overline{T_m^{sp}}$ - $\overline{T_m}$. Units are meters and seconds.

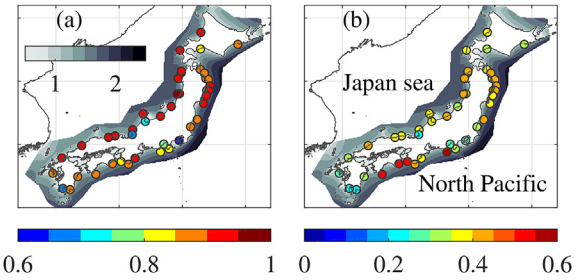

Fig. 3. Comparison of H_s values between hindcast and NOWPHAS buoys. (a) Correlation coefficient and (b) RMSE (unit: m). $\overline{H_s^{sp}}$ drawn in grayscale (unit: m).

A comparison of the hindcast and NOWPHAS T_m values is shown below. Fig. 5(a) and (b) show the correlation coefficient and RMSE of the two-hourly T_m from the hindcast and NOWPHAS. Fig. 5 also shows the $\overline{T_m^{sp}}$ values drawn in grayscale. Based on a comparison of the spectral shapes of the hindcast and NOWPHAS, the hindcast underestimates the windsea when the wave height is low and swells exist. In this situation, the error is relatively large due to the definition of T_m, even if the swell waves are well simulated. Therefore, Fig. 5 comparison is limited to H_s larger than 1 m. Although the correlation coefficients are small compared with H_s, they are greater than 0.8 for the JS and PE regions and 0.7–0.8 for the PW region. The RMSE values are less than 0.8 s and 1.2 s for the JS and Pacific side, respectively. The biases are less than ± 0.6 s (not shown in figure). The results for the three representative locations (Wajima, Hososima, and Kuji), i.e., the JS, PW and PE regions, are shown in detail (Fig. 6). The correlation coefficients are 0.87 (0.89), 0.79 (0.56), and 0.84 (0.74) for Wajima, Hososima, and Kuji, respectively, where the values in parentheses are those that are not limited to the time when H_s is larger than 1 m. The biases are −0.57 (−0.40), −0.30 (0.22), and 0.21 (0.37) s, and the RMSE values are 0.80 (0.76), 1.04 (1.59), and 0.92 (1.24). The percentile values (10, 50, 90, 99, and 99.99 percentiles) indicate good agreement between the shorter (smaller percentile) and longer (larger percentile) wave periods.

Table 1
Location list and percent variance (PV) of EOF modes at each location.

Location	lon	lat	PV (DJF)		PV (JAS)	
			EOF1	EOF2	EOF1	EOF2
No. 1	42.867°N	144.400°E	48	16	44	16
No. 2	40.200°N	141.933°E	47	20	36	16
No. 3	38.200°N	141.667°E	39	21	31	18
No. 4	37.000°N	141.200°E	35	22	32	18
No. 5	35.933°N	140.733°E	39	27	39	18
No. 6	35.000°N	141.000°E	27	20	30	18
No. 7	35.133°N	139.733°E	56	19	45	22
No. 8	34.600°N	138.933°E	42	26	48	17
No. 9	34.867°N	138.533°E	51	19	56	16
No. 10	34.400°N	137.133°E	45	21	44	19
No. 11	33.467°N	135.800°E	49	18	46	20
No. 12	33.600°N	135.267°E	38	25	46	20
No. 13	33.400°N	133.600°E	48	15	49	20
No.14	32.400°N	131.733°E	50	15	49	19
No. 15	32.667°N	129.667°E	50	25	58	14
No. 16	34.000°N	130.467°E	52	16	57	14
No. 17	35.000°N	132.000°E	57	15	43	19
No. 18	35.600°N	133.333°E	45	24	46	15
No. 19	35.600°N	134.133°E	54	19	45	18
No. 20	35.800°N	135.867°E	61	15	42	21
No. 21	37.467°N	136.933°E	53	17	33	27
No. 22	37.400°N	138.200°E	66	12	40	18
No. 23	39.000°N	139.733°E	59	13	52	16
No. 24	40.800°N	139.867°E	52	17	47	15
No. 25	43.867°N	141.467°E	46	26	48	18

These results show that the hindcast around Japan is accurate and can reliably be used in the following wave climate analysis.

3.2. Spectral wave climate: temporal-mean wave spectra

The temporal-mean two-dimensional wave spectra ($\overline{F(\theta,f)}$) are analyzed in this section. The annual mean wave spectra corresponding to data collected over a period of 34 years around Japan are shown in Fig. 7. The precise locations are listed in Table 1. The wave direction (θ)

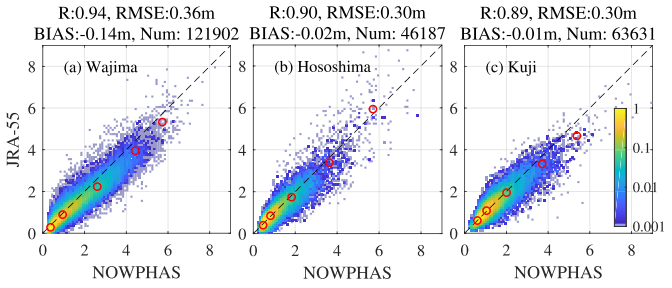

Fig. 4. Comparison of H_s values between hindcast and NOWPHAS buoys at three representative locations (unit: m). Colored shading indicates normalized data density on a $\log_{10}$-scale. Red circles are the percentile values (10, 50, 90, 99, and 99.99 percentiles). (For interpretation of the references to color in this figure legend, the reader is referred to the Web version of this article.)

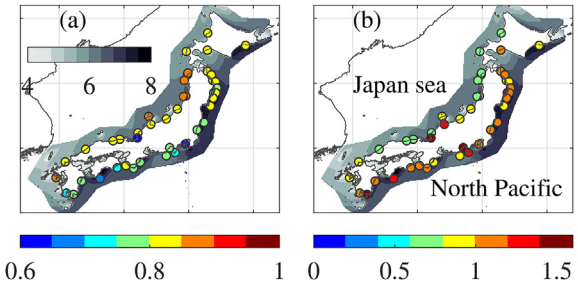

Fig. 5. Same as Fig. 3 but for T_m (unit: s).

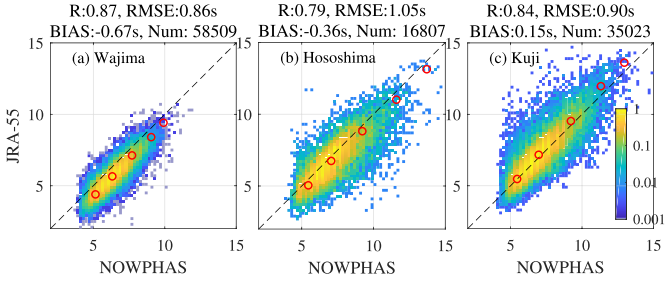

Fig. 6. Same as Fig. 4 but for T_m (unit: s).

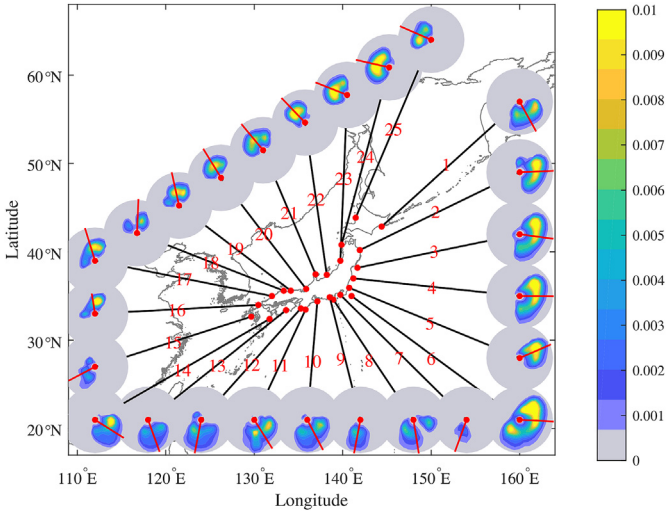

Fig. 7. Annual mean wave spectra over a period of 34 years around Japan (unit: $m^2/(s \cdot rad)$). Red lines indicate $\overline{D_m^{sp}}$. Location information is listed in Table 1. (For interpretation of the references to color in this figure legend, the reader is referred to the Web version of this article.)

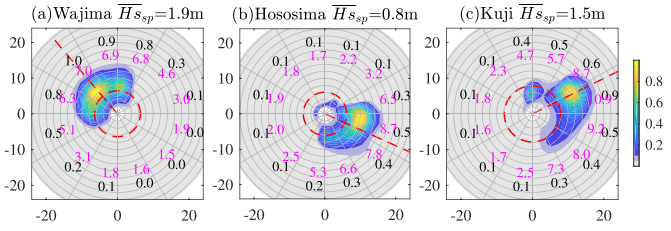

Fig. 8. The winter (DJF) mean wave spectra corresponding to the three representative locations: (a) Wajima (No. 21 in Fig. 7), (b) Hososima (No. 14), and (c) Kuji (No 2). The values are normalized by dividing by the maximum value (maximum value in this figure would be 1). Gray circles correspond to 2 s intervals. Red broken circles and lines represent $\overline{T_m^{sp}}$ and $\overline{D_m^{sp}}$, respectively. The values of $\overline{H_s^{sp}}_{\theta}$ and $\overline{T_m^{sp}}_{\theta}$ for every 30˚are shown by numbers in black and magenta, respectively. (For interpretation of the references to color in this figure legend, the reader is referred to the Web version of this article.)

is defined as the direction from which the wave is coming, clockwise from the north. The radius represents the wave period rather than the frequency, and the energy at the longer radius of the circle represents a long-period wave component. In this discussion, the general spatial characteristics are discussed first, followed by an analysis of the results for specific locations. A distinguishing characteristic of the mean wave spectra in the PE region is a spectral peak in the northeast and its southward extension (Nos. 1–6 in Fig. 7). For the PW region, the mean wave spectra are characterized by bi-modal peaks and long-period components that are generated by TCs (Nos. 7–14). The mean wave spectra for the JS region have relatively narrow band widths for both the period and direction (Nos. 16–25). The annual characteristics shown in Fig. 7 are dominated by summer characteristics for the PW region and winter characteristics for the JS and PE regions.

The results for the three representative locations (Wajima, Hososima, and Kuji, which correspond to Nos. 21, 14, and 2 in Fig. 7) of the JS, PW, and PE regions are shown in detail in the same manner as in the previous section. The $\overline{F(\theta, f)}$ values corresponding to the winter (DJF) and the summer (JAS) are shown in Fig. 8 and Fig. 9, respectively. The $\overline{F(\theta, f)}$ values for Wajima in the winter (the summer) have a peak corresponding to a period of 8.3 (6.2) s and a direction of 310 (10)˚, and the $\overline{H_s^{sp}}$, $\overline{T_m^{sp}}$, and $\overline{D_m^{sp}}$ values are 2.0 (0.9) m, 6.4 (5.1) s and 320 (327)˚, respectively. The seasonal variation in the wave height is large, and the spectral peak shifts in the clockwise direction from the winter to the summer. This clockwise seasonal direction shift can be seen to the west of Wajima (Nos. 18–22), and a counterclockwise shift can be seen to the east of Wajima (Nos. 23–25) in the JS region. It is interesting to note that the seasonal change in the spectral peak direction is large (70 ˚), while in the mean direction it is small (7 ˚).

The $\overline{F(\theta, f)}$ values for Hososima in the winter (the summer) have a peak corresponding to a period of 10.0 (9.1) s and a direction of 100 (100)˚, and the values of $\overline{H_s^{sp}}$, $\overline{T_m^{sp}}$, and $\overline{D_m^{sp}}$ are 1.0 (1.6) m, 6.1 (8.2) s, and 114 (130)˚, respectively. Although there are small differences in the peak and mean directions between the winter and the summer, the energy from the southeast direction is larger in the summer than it is in the winter, which is due to TC generated waves. The $\overline{F(\theta, f)}$ values for Kuji in the winter (the summer) show a peak corresponding to a period of 12.1 (9.1) s and a direction of 60 (100)˚, and the values of $\overline{H_s^{sp}}$, $\overline{T_m^{sp}}$,

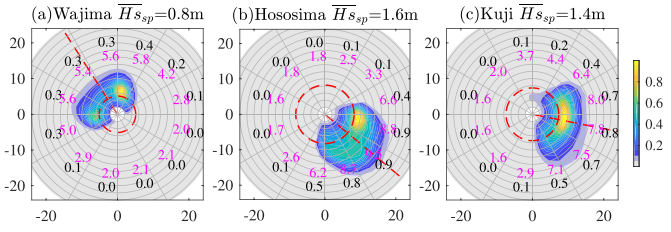

Fig. 9. Same as Fig. 8 but for the summer. (JAS).

and $\overline{D_m^{sp}}$ are 1.6 (1.5) m, 7.8 (7.4) s, and 64 (101)°, respectively. In both the peak direction and the mean direction there is a seasonal variation of 40°. In the winter, the energy is concentrated into long-period waves propagating from the northeast direction, whereas in the summer they propagate from the eastern direction and the degree of concentration of the waves is smaller than it is in the winter.

From Figs. 8 and 9, the directional characteristics can be quantitatively estimated by defining $\overline{H_s^{sp}}$ and $\overline{T_m^{sp}}$ for the target direction (within θ_1 to θ_2) as follows:

$$\bar{H}_{s\,\theta}^{sp} = 4\sqrt{\int\int_{\theta_1}^{\theta_2} F(\bar{\theta},f)d\theta df} = \sqrt{\bar{H}_s^{sp\,2} \times r_{m0}} \tag{6}$$

$$\overline{T_{m\,\theta}^{sp}} = \left(\frac{\int\int_{\theta_1}^{\theta_2} f\bar{F}d\theta df}{\int\int_{\theta_1}^{\theta_2} \bar{F}d\theta df}\right)^{-1} = \overline{T_m^{sp}} \times \frac{r_{m0}}{r_{m1}} \tag{7}$$

where r_{m0} is the ratio of the energy in the target direction to the total energy ($\int\int_{\theta_1}^{\theta_2} \bar{F}d\theta df \;/\; \int\int \bar{F}d\theta df$), and r_{m1} is the ratio of the first order moment in the target direction to the total first order moment ($\int\int_{\theta_1}^{\theta_2} f\bar{F}d\theta df \,/\, \iint f\bar{F}d\theta df$). The values of $\overline{H_{s\,\theta}^{sp}}$ and $\overline{T_{m\,\theta}^{sp}}$ every 30° are shown in Figs. 8 and 9 by numbers in black and magenta, respectively. For example, in the winter at Wajima (Fig. 8(a)), the values of $\overline{H_{s\,\theta}^{sp}}$ and $\overline{T_{m\,\theta}^{sp}}$ between 300 and 330° which include a spectral peak, are 1.0 m ($\overline{H_s^{sp}}$ is 1.9 m) and 7.0 s ($\overline{H_s^{sp}}$ is 6.4 s), respectively. On the other hand, in the summer, the values of $\overline{H_{s\,\theta}^{sp}}$ and $\overline{T_{m\,\theta}^{sp}}$ between 300 and 330 °are 0.3 m and 5.4 s, respectively, which indicate large seasonal differences. The relationships among the wave height, period, and direction can easily be understood according to the above analysis. Therefore, $\overline{F(\theta,f)}$ is useful for describing the wave climate.

3.3. Spectral wave climate: variability in monthly mean spectra

The variability in the monthly mean spectra in the winter and the summer is analyzed using EOF analysis. Table 1 lists the percentages of the variance of the first and second modes (The EOF1 and EOF2) at each location. The percentages of the variance of the EOF1 and EOF2 are from 40 to 50% and approximately 20% (Table 1), respectively. First, the spatial characteristics of the EOF1 and EOF2 are briefly described; a detailed discussion of the EOF1 and EOF2 at representative locations follows. Fig. 10 shows the spectral patterns of the EOF1 and EOF2 in the winter and the summer. Typically, EOF1 is characterized by a uni-modal pattern that is similar to the patterns of the mean spectra ($\overline{F(\theta,f)}$) (Fig. 10(a) (c)). In the JS region (Nos. 17–25), the winter variability is greater than it is in the summer. On the Pacific side (Nos. 1–15, except for No. 5) in the summer season, the variability in the long-period waves propagating from the southern direction is significant. This is considered to be the TC wave variability. Note that the No. 5 location is not open to the south. In the PW region (Nos. 7–15), the summer variability is greater than it is in the winter. EOF2 shows a bi-modal pattern whose peaks are located clockwise and counter-clockwise from the mean wave direction (Fig. 10(b) (d)). EOF1 and 2 correlate strongly with the bulk wave parameters. Table 2 lists the correlation coefficients between the monthly time series of EOF1 (or 2) and the monthly mean bulk wave parameters ($\overline{H_s^{sp}}$, $\overline{T_m^{sp}}$ and $\overline{D_m^{sp}}$). The correlation coefficient between EOF1 and $\overline{H_s^{sp}}$ is high, (approximately 0.9). Thus, EOF1 represents the wave height variability. EOF1 also correlates well with $\overline{T_m^{sp}}$, because wave development is associated with a larger wave height and longer wave period, and $\overline{T_m^{sp}}$ is defined using H_s^2. EOF2 correlates well with $\overline{D_m^{sp}}$. Larger values of EOF1 (Fig. 10(a) and (c)) indicate a larger $\overline{H_s^{sp}}$ variability (variance), and larger values of EOF2 (Fig. 10(b) and (d)) indicate larger $\overline{D_m^{sp}}$ variability (variance). EOF1 and 2 have no correlation. Thus, the correlation between $\overline{H_s^{sp}}$ and $\overline{D_m^{sp}}$ is generally low. If $\overline{D_m^{sp}}$ is regressed on EOF1 and 2, the correlation coefficients associated with the regression increase to above 0.8 at nearly all of the locations. Therefore, EOF1 and 2 represent the variability in the bulk parameters.

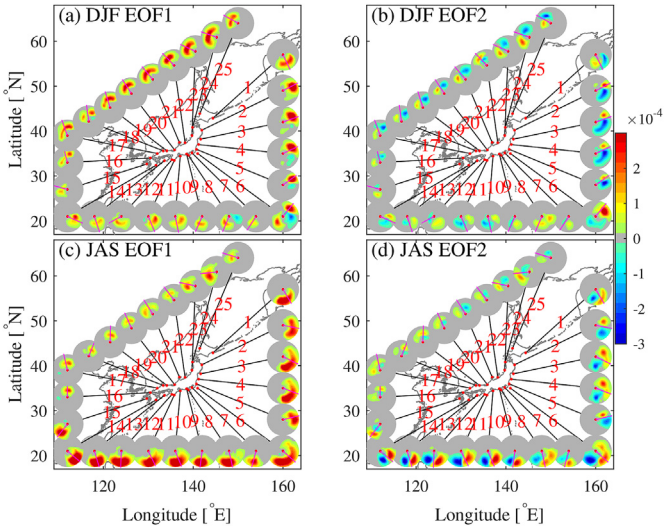

Fig. 10. Spectral patterns of EOF around Japan:(a) EOF1 in the winter, (b) EOF2 in the winter, (c) EOF1 in the summer, and (d) EOF2 in the summer. Red line represents $\overline{D_m^{sp}}$. (unit: m/(s · rad)). (For interpretation of the references to color in this figure legend, the reader is referred to the Web version of this article.)

The relationship between the wave spectral variability and the large-scale atmospheric conditions is shown in Fig. 11 to Fig. 15. The sea level pressure (SLP) and wind vector are used to determine the atmospheric conditions. Three locations are referenced as representatives of the JS, PW, and PE regions in the same manner as in the previous sections. Fig. 11 shows the spectral pattern of EOF1 at Wajima (location No. 21) and the regression map of the SLP and wind vector on the EOF1 monthly time series. A regression map is a map of the slope of a linear regression equation (equation (5)). The spectral pattern of EOF1 (colored shading) is characterized by a variation in the energy of the longer wave component than the spectral peak of the mean spectra, which is drawn using a contour (Fig. 11(a)). The variation in the energy of the longer wave component (rather than the spectral peak) can be considered to be the variation in the magnitude of the wind-wave development. The correlation coefficient between the monthly time series of EOF1 values (eof_1) and $\overline{H_s^{sp}}$ is 0.96, and it is 0.95 for $\overline{T_m^{sp}}$ (Table 2). Therefore, EOF1 largely explains the variability in the wave height and wave period. The EOF1 for Wajima represents the EOF1 variability over nearly the entire JS region (Nos. 16–24) because the correlation coefficient with each location's EOF1 is high, with values greater than 0.7. The center of the SLP variation associated with the EOF1 is located east of Japan (150°E longitude and 40°N latitude). The negative (positive) SLP anomaly leads to a wind speed anomaly in the west or northwest direction (east or northeast direction) in the Japan sea, which leads to larger (smaller) wave energy propagating toward the Japan sea side coast.

Fig. 12 shows the results for Kuji (location No. 2) in the winter. The spectral pattern of EOF1 is similar to the shape of the mean spectra, although it is extended to a longer wave period component (Fig. 12(a)). The correlation coefficient between the monthly time series of EOF1 and $\overline{H_s^{sp}}$ is 0.97, whereas the correlation coefficient between the monthly time series of EOF1 and $\overline{T_m^{sp}}$ is 0.89 (Table 2). The EOF1 for Kuji represents the EOF1 variability for the PE region (Nos. 2–5), because the correlation coefficients are high, with values greater than 0.8. The centers of the SLP variations associated with the EOF1 are located over the Bering Sea and the mid-latitudes of the North Pacific. The positive (negative) SLP anomaly over the Bering Sea and negative (positive) SLP anomaly over the mid-latitudes lead to an anomaly in the wind speed from the eastern direction (western) near the Aleutian Islands, which leads to a larger (smaller) swells propagating from the Aleutian Islands region to the PE region. Fig. 12(b) also shows the great

Table 2
Correlation coefficients between EOF values and bulk parameters ($\overline{H_s^{sp}}$, $\overline{T_m^{sp}}$ and $\overline{D_m^{sp}}$).

Location	DJF						JAS					
	Hs		Tm		Dm		Hs		Tm		Dm	
	1	2	1	2	1	2	1	2	1	2	1	2
No. 1	0.98	0.03	0.76	0.29	0.22	0.85	0.94	0.03	0.95	0.13	0.29	0.83
No. 2	0.97	0.14	0.89	0.01	0.26	0.76	0.96	0.01	0.86	0.15	0.19	0.89
No. 3	0.93	0.30	0.87	0.09	0.31	0.78	0.93	0.11	0.91	0.15	0.16	0.92
No. 4	0.86	0.45	0.88	0.11	0.41	0.72	0.94	0.13	0.89	0.17	0.19	0.91
No. 5	0.83	0.50	0.93	0.03	0.11	0.78	0.96	0.01	0.73	0.06	0.28	0.83
No. 6	0.53	0.45	0.56	0.62	0.47	0.26	0.93	0.05	0.90	0.00	0.06	0.79
No. 7	0.99	0.06	0.71	0.39	0.14	0.85	0.90	0.26	0.81	0.27	0.23	0.75
No. 8	0.63	0.72	0.27	0.81	0.71	0.57	0.94	0.06	0.93	0.16	0.33	0.81
No. 9	0.98	0.10	0.77	0.36	0.33	0.85	0.96	0.09	0.93	0.11	0.16	0.76
No. 10	0.92	0.32	0.90	0.14	0.75	0.49	0.96	0.06	0.91	0.11	0.12	0.81
No. 11	0.89	0.38	0.88	0.08	0.77	0.47	0.96	0.06	0.93	0.01	0.15	0.84
No. 12	0.94	0.24	0.87	0.31	0.69	0.53	0.96	0.07	0.94	0.05	0.06	0.78
No. 13	0.98	0.08	0.69	0.25	0.39	0.70	0.97	0.06	0.90	0.14	0.02	0.82
No. 14	0.99	0.09	0.85	0.02	0.11	0.50	0.97	0.06	0.88	0.22	0.02	0.85
No. 15	0.98	0.01	0.80	0.37	0.39	0.83	0.95	0.17	0.92	0.08	0.49	0.24
No. 16	0.93	0.32	0.69	0.22	0.63	0.65	0.96	0.12	0.87	0.27	0.48	0.53
No. 17	0.96	0.11	0.75	0.54	0.64	0.71	0.89	0.34	0.79	0.35	0.56	0.66
No. 18	0.87	0.28	0.68	0.62	0.58	0.78	0.98	0.01	0.78	0.36	0.34	0.34
No. 19	0.95	0.14	0.79	0.48	0.52	0.81	0.97	0.03	0.83	0.32	0.37	0.52
No. 20	0.96	0.11	0.92	0.14	0.53	0.79	0.96	0.09	0.85	0.13	0.14	0.78
No. 21	0.96	0.16	0.95	0.17	0.55	0.73	0.88	0.39	0.78	0.21	0.39	0.81
No. 22	0.96	0.23	0.95	0.10	0.42	0.40	0.97	0.05	0.82	0.09	0.14	0.83
No. 23	0.97	0.12	0.95	0.03	0.33	0.85	0.95	0.27	0.85	0.05	0.52	0.57
No. 24	0.97	0.13	0.96	0.05	0.29	0.88	0.95	0.15	0.93	0.06	0.57	0.20
No. 25	0.97	0.07	0.88	0.23	0.02	0.92	0.95	0.26	0.89	0.04	0.47	0.75

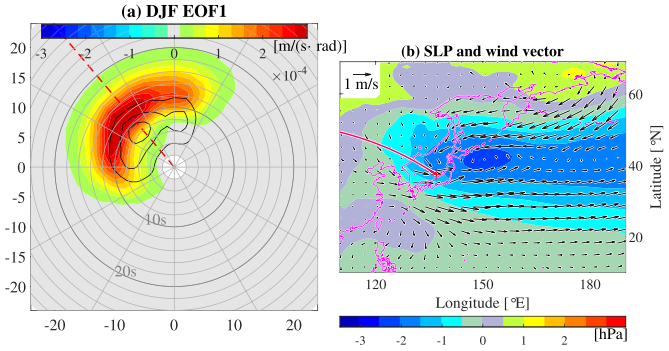

Fig. 11. (a) Spectral pattern of EOF1 in the winter at Wajima (location No. 21) and (b) regression map of SLP and wind vector on EOF1 monthly time series. The color shading and contour in panel (a) represent the EOF and mean spectra as in Fig. 8(a), respectively. Contour lines are 0.2, 0.5, and 0.8. Red dashed line indicates $\overline{D_m^{sp}}$. The colored shading and arrows in panel (b) represent the SLP (unit: hPa) and wind vector, respectively. The location of Wajima is shown by a red plus mark in panel (b). The red line in panel (b) is the great circle path starting from Wajima, with the peak direction of EOF1. (For interpretation of the references to color in this figure legend, the reader is referred to the Web version of this article.)

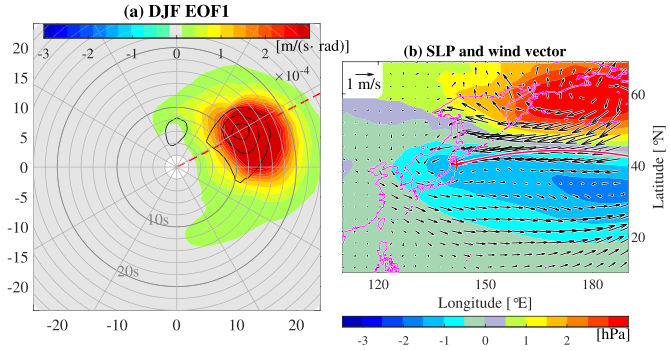

Fig. 12. Same as Fig. 11 but for EOF1 in the winter at Kuji (location No. 2).

circle path starting from Kuji with the direction of peak of EOF1 shown by Fig. 12(a). The great circle path represents the swell propagation path from the Aleutian Islands region to the PE region.

The spectral pattern of the EOF2 for Kuji in the winter is bi-modal (Fig. 13(a)). This explains the variance of $\overline{D_m^{sp}}$ whose standard deviation is 12°; the correlation coefficient between EOF2 and $\overline{D_m^{sp}}$ is 0.76 (Table 2). The center of the SLP variance associated with the EOF2 is located at a latitude of approximately 40°N in the central North Pacific (Fig. 13(b)). The negative (positive) SLP anomaly leads to a wind speed anomaly in the northeast direction at a latitude of approximately 50°N (in the southeast direction at a latitude of 30°N) and a longitude of approximately 150°E, which leads to northerly (southerly) wave energy propagating toward the PE region (Fig. 13(a) and Nos. 2–5 in

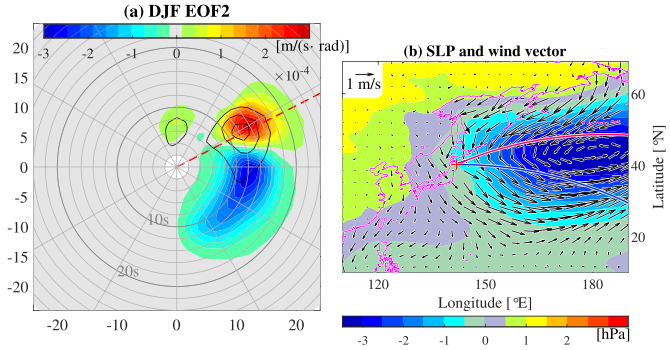

Fig. 13. Same as Fig. 11 but for EOF2 in the winter at Kuji (location No. 2). The red and blue lines in panel (b) are the great circle paths starting from Kuji with the positive and negative peak directions of EOF2. (For interpretation of the references to color in this figure legend, the reader is referred to the Web version of this article.)

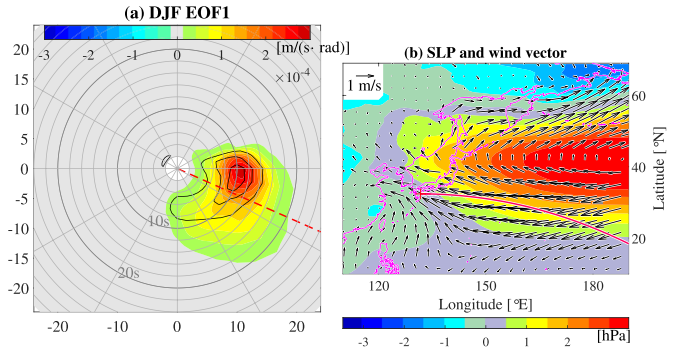

Fig. 14. Same as Fig. 11 but for EOF1 in the winter at Hososima (location No. 14).

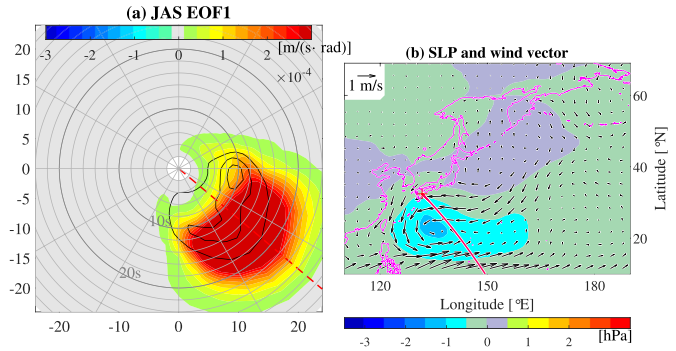

Fig. 15. Same as Fig. 11 but for EOF1 in the summer at Hososima (location No. 14).

Fig. 10(b)). This results in a northeasterly to southeasterly wave direction variance. The northeasterly and southeasterly wave propagation paths (great circle paths with the direction of positive and negative peaks of the EOF2) are plotted using red and blue lines in Fig. 13(b).

The atmospheric conditions corresponding to EOF2 in the PE region are also related to EOF1 in the PW region, as explained below. Fig. 14 shows the EOF1 results for Hososima (location No. 14) in the winter. The spectral pattern of EOF1 is similar to the shape of the mean spectra (Fig. 14(a)). The correlation coefficient between the monthly time series of EOF1 and $\overline{H_s^{sp}}$ is 0.99, with a value for $\overline{T_m^{sp}}$ of 0.88 (Table 2). The EOF1 for Hososima represents that of the PE region (Nos. 10–14, except for 12), because the correlation coefficient with each location's EOF1 time series is greater than 0.8. Location No. 12 is not open to the east. The regression map (Fig. 14(b)) is similar to that of EOF2 for the PE region (Fig. 13(b)), whose regression map is characterized by the SLP variation over the central North Pacific. Note that the sign (positive or negative) is reversed, but this does not matter here. The positive (negative) SLP anomaly leads to an eastern (western) wind speed anomaly at a latitude of 30°N over the North Pacific, which leads to larger (smaller) swells propagating from the east toward the PW region (Fig. 14(a) and Nos. 10–14, except for No. 12 in Fig. 10(b)). The EOF1 for location No. 12 is different than those for Nos. 10–14, even though they are all located in the PW region, because swells propagating from the east are the primary components of the variability for Nos. 10–14, and No. 12 is not open to the east. Again, the regression map (Fig. 14(b)) is similar to that for EOF2 in the PE region (Fig. 13(b)). The correlation coefficients between EOF1 for Hososima and EOF2 for the PE region have values of 0.52–0.65. It is interesting to note that the wave height variability is closely related to the wave direction variability for locations 1 000 km apart via the SLP variance over the North Pacific.

The winter variability in the spectral wave climate associated with large-scale (North Pacific) atmospheric conditions is described above. Here, we discuss the effects of TC-generated waves, which are significant in the summer, particularly along the Pacific coast. Fig. 15 shows the results for Hososima in the summer. The correlation coefficient between the monthly time series of EOF1 and $\overline{H_s^{sp}}$ is 0.97; the correlation coefficient between the monthly time series of EOF1 and $\overline{T_m^{sp}}$ is 0.88 (Table 2). The correlation coefficients for EOF1 of Hososima with other PW locations (Nos. 6–13) have values between 0.79 and 0.95. Therefore, the variability shown by Fig. 15 is characteristic of the PW region in the summer. The spectral pattern for the EOF1 differs from the shape of the mean spectra (Fig. 15(a)). The mean spectra (contour in Fig. 15(a)) has a peak from the western direction. However, the peak for EOF1 is from the southern direction and has a longer wave period. This is due to the large variability in the TC-generated swells. The TC signature can be seen in the regression map (Fig. 15(b)), which shows the SLP variation over the lower latitudes of the western North Pacific. The center of the SLP variance is located at the lower latitudes of the western North Pacific, which is the active TC region. The variability in the TC-generated swells in this region has a significant impact on the variability in the wave climate in the PW region. Furthermore, the EOF1 along the PE region is strongly related to the variability in the TC-generated swells, even though the center of the SLP variance is located east of Fig. 15(b) (not shown).

4. Conclusions

In this study, a high-resolution wave climate hindcast along the Japanese coast is presented. This hindcast is a subset of the global one developed by Mori et al. (2017). The spectral wave model WAVEWATCH III was forced using the sea surface wind and sea ice concentration data from the JRA-55 atmospheric reanalysis. The computational period is 34 years (1979–2012). The three domains were chosen using a nesting process and included the North Pacific domain (spatial resolution: 30 min), western North Pacific domain (10 min), and Japanese coastal domain (4 min). The high-resolution wave climate hindcast was carefully compared with NOWPHAS buoy observations around Japan. The correlation coefficient, RMSE, and bias of H_s are 0.9, 0.5–0.7 m, and −0.4 to 0.15 m, respectively. The correlation coefficients of T_m are 0.8 for the JS and PE regions and 0.7–0.8 for the PW region. The RMSE values are under 0.8 s and 1.2 s for the Japan Sea and Pacific side, respectively. The biases are less than ± 0.6 s. Based on the close agreement between our hindcast and the observations, we consider our wave climate hindcast around Japan to be reliable for wave climate analysis.

The wave climate around Japan is represented using temporal-mean two-dimensional (frequency-direction) wave spectra. Temporal-mean bulk wave parameters are also defined using the mean wave spectra, which are equal to the mean values weighted by squared H_s. The wave spectra-based mean bulk wave parameter represents the mean wave state (wave climate) more appropriately than the ordinary mean does. The characteristics of the spectral wave climate around Japan are discussed by classifying them into three types. The general characteristics of the mean wave spectra along the JS region are narrow band widths for both the period and the direction. The mean wave spectra along the PE region are characterized by swells with a spectral peak in the northeast direction. In the PW region, the mean wave spectra are characterized by bi-modal peaks and long-period components, which are generated by the TCs. The annual characteristics are dominated by the summer characteristics for the PW region, and the JS and PE regions display the winter characteristics.

The variability in the mean wave spectra is analyzed using an EOF analysis. The EOF1 of the monthly mean wave spectra represents the variability in the mean wave height ($\overline{H_s^{sp}}$) and mean wave period ($\overline{T_m^{sp}}$). EOF2 is closely related to the variability in the mean wave direction ($\overline{D_m^{sp}}$). The winter EOF1 values for the JS locations are characterized by the variability in the magnitude of wind-wave development and are associated with the SLP variance just east of Japan. The winter EOF1 values for the PE locations are characterized by the variability in the swells coming from the northeast direction and are associated with the

SLP variance at higher latitudes of the North Pacific. On the other hand, the EOF2 values of the PE region representing the variability in the wave direction are associated with the SLP variance over the central North Pacific. Furthermore, the EOF2 values for the PE region are related to the EOF1 values for the PW region via the SLP variance over the central North Pacific. The winter EOF1 values for the PW locations are characterized by the variability in swells coming from the eastern direction. In the summer, the EOF1 values for the Pacific side locations are dominated by the variability in the TC-generated swells. The spectral wave climate representation in this study provides clear insight into the wave climate around Japan because the relationships between the atmospheric conditions, the wave height, direction, and period are easy to understand.

Acknowledgement

NM is supported by JSPS KAKENHI Grant Number 16H04416. This research is supported under the TOUGOU Program by the Ministry of Education, Culture, Sports, Science, and Technology (MEXT).

Appendix A. Supplementary data

Supplementary data to this article can be found online at https://doi.org/10.1016/j.coastaleng.2019.04.013.

References

Ardhuin, F., Rogers, E., Babanin, A.V., Filipot, J.F., Magne, R., Roland, A., Van Der Westhuysen, A., Queffeulou, P., Lefevre, J.M., Aouf, L., et al., 2010. Semiempirical dissipation source functions for ocean waves. Part I: definition, calibration, and validation. J. Phys. Oceanogr. 40, 1917–1941.

Barnard, P.L., Short, A.D., Harley, M.D., Splinter, K.D., Vitousek, S., Turner, I.L., Allan, J., Banno, M., Bryan, K.R., Doria, A., et al., 2015. Coastal vulnerability across the pacific dominated by el niño/southern oscillation. Nat. Geosci. 8, 801–807.

Boukhanovsky, A.V., Lopatoukhin, L.J., Soares, C.G., 2007. Spectral wave climate of the north sea. Appl. Ocean Res. 29, 146–154.

Bromirski, P.D., Cayan, D.R., Flick, R.E., 2005. Wave spectral energy variability in the northeast pacific. J. Geophys. Res.: Oceans 110.

Buckley, W.H., 1988. Extreme and climatic wave spectra for use in structural design of ships. Nav. Eng. J. 100, 36–58.

Chawla, A., Spindler, D.M., Tolman, H.L., 2013. Validation of a thirty year wave hindcast using the climate forecast system reanalysis winds. Ocean Model. 70, 189–206.

Dee, D.P., Uppala, S., Simmons, A., Berrisford, P., Poli, P., Kobayashi, S., Andrae, U., Balmaseda, M., Balsamo, G., Bauer, d.P., et al., 2011. The era-interim reanalysis: configuration and performance of the data assimilation system. Q. J. R. Meteorol. Soc. 137, 553–597.

Durrant, T., Greenslade, D., Hemer, M., Trenham, C., 2014. A Global Wave Hindcast Focussed on the Central and South Pacific, vol. 40.

Elshinnawy, A.I., Medina, R., González, M., 2017. On the relation between the direction of the wave energy flux and the orientation of equilibrium beaches. Coast Eng. 127, 20–36.

Gainza, J., González, E.M., Medina, R., 2018. A process based shape equation for a static equilibrium beach planform. Coast Eng. 136, 119–129.

Gouldby, B., Méndez, F., Guanche, Y., Rueda, A., Minguez, R., 2014. A methodology for deriving extreme nearshore sea conditions for structural design and flood risk analysis. Coast Eng. 88, 15–26.

Hamilton, L., 2010. Characterising spectral sea wave conditions with statistical clustering of actual spectra. Appl. Ocean Res. 32, 332–342.

Hatada, Y., Yamaguchi, M., 2002. Estimation of long-term variability of wave climate around the coastal sea areas of Japan. In: Proceedings of the 28th International Conderence of Coastal Engineering, pp. 61–73.

Hemer, M.A., Fan, Y., Mori, N., Semedo, A., Wang, X.L., 2013. Projected changes in wave climate from a multi-model ensemble. Nat. Clim. Change 3, 471.

Holthuijsen, L.H., 2010. Waves in Oceanic and Coastal Waters. Cambridge university press.

Innocentini, V., Caetano, E., Carvalho, J.T., 2014. A procedure for operational use of wave hindcasts to identify landfall of heavy swell. Weather Forecast. 29, 349–365.

Kobayashi, S., Ota, Y., Harada, Y., Ebita, A., Moriya, M., Onoda, H., Onogi, K., Kamahori, H., Kobayashi, C., Endo, H., et al., 2015. The jra-55 reanalysis: general specifications and basic characteristics. J. Meteorol. Soc. Jpn. Ser. II 93, 5–48.

Lucas, C., Boukhanovsky, A., Soares, C.G., 2011. Modeling the climatic variability of directional wave spectra. Ocean Eng. 38, 1283–1290.

Melet, A., Meyssignac, B., Almar, R., Le Cozannet, G., 2018. Under-estimated wave contribution to coastal sea-level rise. Nat. Clim. Change 8, 234.

Mentaschi, L., Vousdoukas, M.I., Voukouvalas, E., Dosio, A., Feyen, L., 2017. Global changes of extreme coastal wave energy fluxes triggered by intensified teleconnection patterns. Geophys. Res. Lett. 44, 2416–2426.

Mori, N., Shimura, T., Kamahori, H., Chawla, A., 2017. Histrical Wave Climate Hindcasts Based on Jra-55. Coatal Dynamics 2017.

Morim, J., Cartwright, N., Etemad-Shahidi, A., Strauss, D., Hemer, M., 2016. Wave energy resource assessment along the southeast coast of Australia on the basis of a 31-year hindcast. Appl. Energy 184, 276–297.

Nagai, T., 1997. Study on Japanese coastal wave characteristics obtained from the nowphas wave observation network. In: Technical Note of the Port and Harbour Research Institute.

Perez, J., Menendez, M., Losada, I.J., 2017. Gow2: a global wave hindcast for coastal applications. Coast Eng. 124, 1–11.

Portilla-Yandún, J., 2018. The global signature of ocean wave spectra. Geophys. Res. Lett. 45, 267–276.

Portilla-Yandún, J., Cavaleri, L., Van Vledder, G.P., 2015. Wave spectra partitioning and long term statistical distribution. Ocean Model. 96, 148–160.

Portilla-Yandún, J., Salazar, A., Cavaleri, L., 2016. Climate patterns derived from ocean wave spectra. Geophys. Res. Lett. 43.

Rascle, N., Ardhuin, F., 2013. A global wave parameter database for geophysical applications. part 2: model validation with improved source term parameterization. Ocean Model. 70, 174–188.

Saha, S., Moorthi, S., Pan, H.L., Wu, X., Wang, J., Nadiga, S., Tripp, P., Kistler, R., Woollen, J., Behringer, D., et al., 2010. The ncep climate forecast system reanalysis. Bull. Am. Meteorol. Soc. 91, 1015–1058.

Sasaki, W., 2012. Changes in wave energy resources around Japan. Geophys. Res. Lett. 39.

Semedo, A., Sušelj, K., Rutgersson, A., Sterl, A., 2011. A global view on the wind sea and swell climate and variability from era-40. J. Clim. 24, 1461–1479.

Shimura, T., Mori, N., Mase, H., 2013. Ocean waves and teleconnection patterns in the northern hemisphere. J. Clim. 26, 8654–8670.

Shimura, T., Mori, N., Hemer, M.A., 2016. Variability and future decreases in winter wave heights in the western north pacific. Geophys. Res. Lett. 43, 2716–2722.

Stopa, J.E., Cheung, K.F., Tolman, H.L., Chawla, A., 2013. Patterns and cycles in the climate forecast system reanalysis wind and wave data. Ocean Model. 70, 207–220.

Tolman, H., 2014. User Manual and System Documentation of WAVEWATCH III Version 4.18 NOAA/NWS/NCEP/MMAB Technical Note 316.

van Nieuwkoop, J.C., Smith, H.C., Smith, G.H., Johanning, L., 2013. Wave resource assessment along the Cornish coast (UK) from a 23-year hindcast dataset validated against buoy measurements. Renew. Energy 58, 1–14.

Von Storch, H., Zwiers, F., 2002. Statistical Analysis in Climate Research. Cambridge University Press.

Yates, M.L., Le Cozannet, G., Garcin, M., Salaï, E., Walker, P., 2013. Multidecadal atoll shoreline change on manihi and manuae, French polynesia. J. Coast. Res. 29, 870–882.

Young, I., Zieger, S., Babanin, A.V., 2011. Global trends in wind speed and wave height. Science 332, 451–455.